Journal of Biomedical Optics

SPIEDigitalLibrary.org/jbo

Catheter-based photoacoustic endoscope

Joon-Mo Yang
Chiye Li
Ruimin Chen
Qifa Zhou
K. Kirk Shung
Lihong V. Wang

SPIE

Catheter-based photoacoustic endoscope

Joon-Mo Yang,[a,†] Chiye Li,[a,†] Ruimin Chen,[b] Qifa Zhou,[b] K. Kirk Shung,[b] and Lihong V. Wang[a,*]
[a]Washington University in St. Louis, Department of Biomedical Engineering, Optical Imaging Laboratory, Campus Box 1097, One Brookings Drive, Street Louis, Missouri 63130
[b]University of Southern California, NIH Ultrasonic Transducer Resource Center, Department of Biomedical Engineering, 1042 Downey Way, University Park, Drive 130, Los Angeles, California 90089

Abstract. We report a flexible shaft-based mechanical scanning photoacoustic endoscopy (PAE) system that can be potentially used for imaging the human gastrointestinal tract via the instrument channel of a clinical video endoscope. The development of such a catheter endoscope has been an important challenge to realize the technique's benefits in clinical settings. We successfully implemented a prototype PAE system that has a 3.2-mm diameter and 2.5-m long catheter section. As the instrument's flexible shaft and scanning tip are fully encapsulated in a plastic catheter, it easily fits within the 3.7-mm diameter instrument channel of a clinical video endoscope. Here, we demonstrate the intra-instrument channel workability and *in vivo* animal imaging capability of the PAE system. [DOI: 10.1117/1.JBO.19.6.066001]

Keywords: photoacoustic endoscopy; flexible shaft; catheter endoscope; instrument channel; gastrointestinal endoscopy; rabbit esophagus; *in vivo* imaging.

Paper 140033R received Jan. 20, 2014; revised manuscript received Apr. 26, 2014; accepted for publication May 6, 2014; published online Jun. 2, 2014.

1 Introduction

Minimally invasive imaging applications of photoacoustic (PA) tomography[1–6] are emerging as a new research area in biomedical photoacoustics. PA tomography is expected to be a useful tool in the clinic because it enables high-resolution tomographic imaging at depths beyond the optical diffusion limit (~1 mm in scattering tissue) and provides a wealth of functional and molecular information based on its strong spectroscopic imaging capability.[1–14] So far, the clinical potential of the technique has been investigated in various endoscopic areas.[15–26] However, the development of associated imaging devices is still at an immature stage because of technical challenges. Unlike existing ultrasonic (US)[27,28] or optical endoscopic probes,[29–37] PA endoscopy (PAE) requires the integration of both optical and acoustic elements in a small space. Also, in the case of a single element-based mechanical scanning endoscope, its internal space must be filled with an acoustic matching medium whose acoustic and optical properties must be considered carefully. Such requirements present difficult challenges in the development of a suitable probe.

In 2009, we implemented a 4.2-mm diameter PA endoscope and demonstrated its feasibility for PAE.[15] To solve the aforementioned technical issues, we employed a rotating scanning mirror driven by a built-in micromotor. The main advantage of this probe configuration is that it enables static mounting of the optical fiber and signal wires, thereby facilitating the optical and acoustical integration and providing a simple solution to the acoustic matching requirement. As the performance of the prototype endoscope was satisfactory, we developed a 3.8-mm diameter probe[17] with the same probe configuration. In addition to reducing the size of the probe, we also improved the image resolution by using a focused US transducer.[16] With this probe, we demonstrated simultaneous dual-wavelength PA and US endoscopy for the first time through *in vivo* animal experiments.[17] After the *in vivo* demonstration, we proceeded to develop a 2.5-mm diameter miniprobe to increase the clinical applicability of the PAE technique.[18] Our goal was to use the miniprobe for imaging human upper gastrointestinal (GI) tracts with Barrett's esophagus via the 3.7-mm diameter instrument channel of a clinical video endoscope. However, the sharply bent section of the entry port precluded normal insertion of the 35-mm long rigid distal section that includes a micromotor. To avoid this bend, the probe had to be inserted in reverse through the exit port. Thus, we concluded that the probe was suitable only for lower GI tract imaging.

For imaging the human esophagus, it is essential to use a video endoscope for image guidance to approach the target organ safely. Thus, the PAE probe must be narrow and flexible to pass through the instrument channel of the video endoscope freely. The probe must also be fully encapsulated to avoid direct contact of the scanning tip with the target tissue during mechanical scanning. To meet these technical requirements, we have designed and implemented a new catheter-based PAE system and demonstrated its endoscopic functionality through the instrument channel. This endoscopic system is based on mechanical scanning of a single-element US transducer. Its flexible catheter section, 3.2-mm in outer diameter and 2.5-m in length, can be inserted into a 3.7-mm diameter instrument channel. This prototype features a flexible shaft-based proximal actuation mechanism, such as commercial endoscopic ultrasound miniprobes,[27,28] and a laser beam delivery through a rotary junction, such as endoscopic optical coherence tomography catheters.[29–34] To the best of our knowledge, this is the first PAE system that has been fully encapsulated in a plastic catheter and sufficiently miniaturized to be usable for imaging via the instrument channel of a standard clinical endoscope. Here, we describe the detailed structure and fabrication of the new

*Address all correspondence to: Lihong V. Wang, E-mail:lhwang@biomed.wustl.edu

†These authors contributed equally to this work.

0091-3286/2014/$25.00

PAE system and present experimental results demonstrating its full intra-instrument channel workability and *in vivo* imaging capability.

2 Design and Construction of the Catheter-Based PAE System

2.1 *System Composition and Operating Principles*

Figure 1 shows schematic diagrams and photos of the implemented PAE system. As presented in Fig. 1(a), the endoscopic system is comprised of a proximal actuation unit, a ~2.5-m long flexible body section sheathed with a plastic catheter, and a rigid distal section that includes a scanning mirror. A step motor installed in the proximal actuation unit provides torque. The torque is transferred to a hollow metal shaft supported by two ball bearings through a timing belt and pulleys and further transmitted to the scanning mirror through the 2.5-m long flexible shaft (TC+2113-70-2600-01, Asahi Intecc, Burlington). Finally, the scanning mirror receives the torque and performs side-view rotational scanning.

For PA imaging, a pulsed laser beam from a laser source (Nd:YVO4, INNOSLAB IS811-E, EdgeWave, Würselen, Germany) is guided by a multimode optical fiber (~5-m long, 0.22 NA, 365-μm core diameter, BFL22-365, Thorlabs, Newton, New Jersey) and is transferred via a rotary junction [Fig. 1(a)] to the endoscope's optical fiber (same type, ~2.5-m long) located inside the flexible shaft, sent to the target tissue by the optics located in the scanning mirror to generate PA waves. The generated PA waves that propagate to the scanning mirror are reflected to a focused US transducer (1.7-mm aperture, f = 5-mm, NA = 0.17, 40 MHz) and converted into electrical signals. Figures 1(b) and 1(c) show the entire endoscopic system and the distal section of the probe.

In Figs. 1(d) and 1(e), we present a more detailed structure of the rigid distal section [Fig. 1(c)] and photos of several key components, respectively. The rigid distal section is ~16-mm long, and its housing was fabricated from a 3.05-mm diameter stainless steel tube (wall thickness: 0.33-mm). Inside the housing, the scanning mirror (2.1-mm outer diameter) and the focused US transducer (2.1-mm outer diameter) are encapsulated as shown in Fig. 1(d). To provide a smooth rotation to the scanning mirror, we utilized a bronze sleeve bearing and placed bushings at the sleeve bearing's ends to eliminate longitudinal movement of the scanning mirror. The bronze sleeve bearing also acts as a joint connecting the rigid distal section and the plastic catheter (3.18-mm outer diameter and 1.59-mm inner diameter) made of polytetrafluoroethylene (PTFE, Zeus, Orangeburg). The scanning mirror is mechanically coupled to the flexible shaft via a narrow-diameter stainless steel tubular shaft (~0.81-mm outer diameter).

The optical fiber's tip [Fig. 1(d)] is polished at an ~30-deg angle, and the scanning mirror's inner space is filled with air, so that the laser beam that impinges on the polished fiber surface experiences an optical total internal reflection (TIR), and it exits the fiber with an oblique angle of ~43 deg. The laser beam is then reflected by a dielectric-coated borofloat mirror (altered

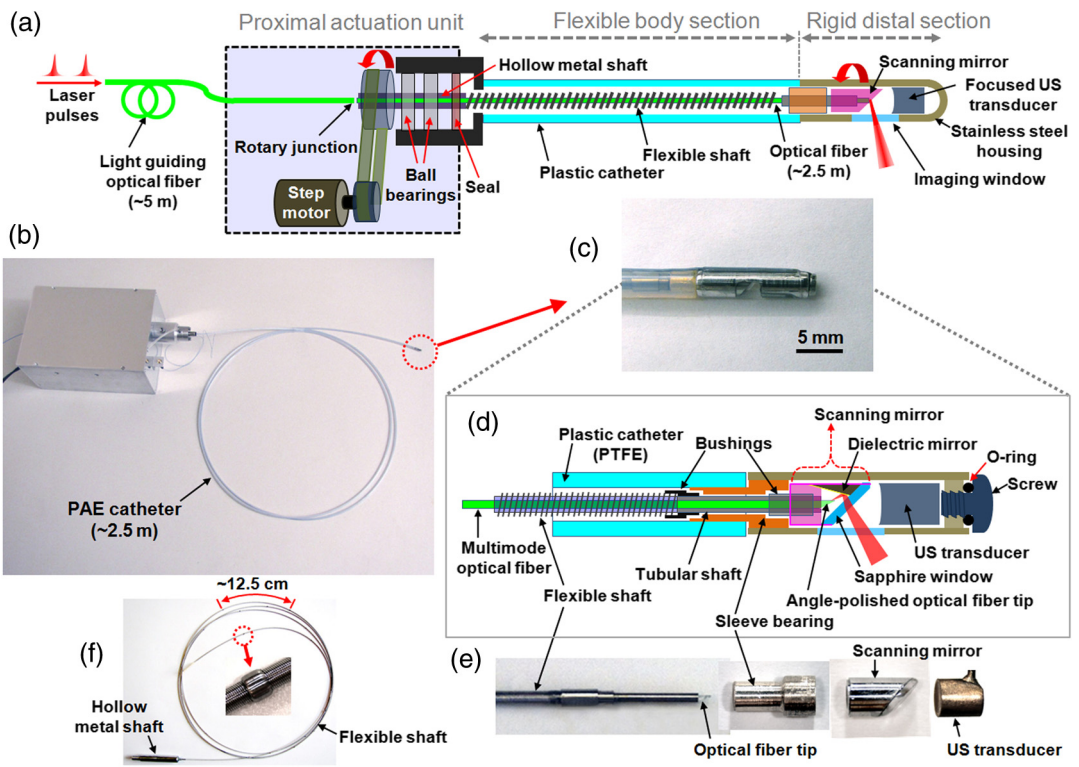

Fig. 1 (a) Schematic of the catheter-based photoacoustic endoscopy (PAE) system. (b) Photo of the entire endoscopic system. (c) Photo of the rigid distal section. (d) Schematic showing the detailed structure of the rigid distal section presented in (c). (e) Photos of the flexible shaft and optical fiber tip, the bronze sleeve bearing, the scanning mirror, and the focused US transducer. (f) Photo of the 2.5-m long flexible shaft connected to the hollow metal shaft depicted in (a). The inset represents a magnified sleeve bearing.

from #45-596, Edmund, Barrington) and finally sent to the target tissue after passing through an optically transparent sapphire window (altered from #43-627, Edmund) and an optically clear polyethylene terephthalate (PET) plastic membrane (~3-mm inner diameter, ~25-μm wall thickness, 103-0380, Advanced Polymers, Salem). The PET membrane, a medical grade plastic, forms an imaging window by sealing the inner cavity of the stainless steel housing. (More details of the optical components and laser beam path are presented in Sec. 2.2).

To provide acoustic matching from the imaging window to the US transducer [Fig. 1(d)], we filled the inner cavity of the endoscope with deionized water (details are given in Sec. 2.5). Also, we used sapphire for the optical window of the scanning mirror because it has an adequate thickness (0.5-mm) and high acoustic impedance (44.3 MRayl) for perfect TIR (Ref. 15) of the approaching acoustic waves within the acceptance angle of the US transducer. The 0.5-mm thickness is ~1.8 times larger than the wavelength of the 40 MHz acoustic waves, and the ratio of sound propagation speeds in water and sapphire is 1.5/11.1 for longitudinal waves.

In Fig. 1(e), we show the components of the rigid distal section, including the flexible shaft and optical fiber tip, the bronze sleeve bearing, the scanning mirror, and the focused US transducer. Figure 1(f) shows the entire flexible shaft; its proximal end is connected to the hollow metal shaft [Fig. 1(a)], and its distal end, which corresponds to the optical fiber tip, is shown in Fig. 1(e). As shown in the inset, we affixed stainless steel sleeve bearings around the surface of the flexible shaft at ~12.5-cm intervals to minimize mechanical friction during its rotation. To assemble the components, we utilized medical grade epoxies, such as M-31CL (Loctite) and DP-125 (3M).

Figure 2 shows the interior of the proximal actuation unit [Fig. 1(a)]. To control the step motor's rotation speed, we employ a function generator (SFG-2110, GWInstek, Chino) that provides transistor-transistor logic (TTL) signals with a continuously variable frequency. The function generator's TTL signals trigger the step motor's driver circuit as well as the laser system and a data acquisition (DAQ) card (NI PCI-5124, National Instruments, Austin). Once an endoscopic imaging session is initiated, we slowly dial the function generator's TTL frequency to a desired value and then transmit the TTL signals to the laser system; we activate our DAQ program immediately. The acquired PA images are displayed on the computer screen in real time. For PA imaging, we utilized a 532-nm laser wavelength (~10-ns pulse duration) with a pulse energy of ~0.25 mJ. The laser beam delivered by the 5-m long guiding optical fiber was coupled to the endoscope's 2.5-m long optical fiber via the rotary junction. The inset shows the rotary junction, in which one can see two glass ferrules that enclose the 2.5 and 5-m optical fibers. We set the number of A-lines for one full B-scan to be 400, which yields an angular step size of 0.9 deg.

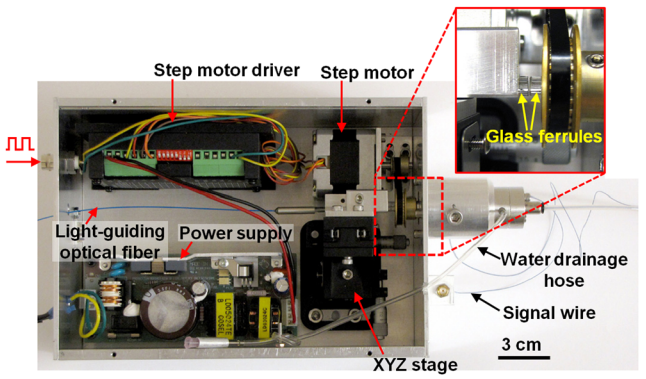

Fig. 2 Photos of the proximal actuation unit. The inset shows a magnified view of the rotary junction formed for coupling the two multimode optical fibers. The optical fibers are placed inside the two glass ferrules.

2.2 *Detailed Configuration of Optical and Acoustic Components at the Rigid Distal End*

To induce PA signals, an adequate level of laser energy must be delivered to the target tissue via the narrow area of the scanning mirror. As a high-laser flux and a high-pulse repetition rate can result in gradual degradation of the optical components, the optics need to be carefully designed. In addition, it is important to configure the optical illumination and acoustic detection units of the rigid distal section appropriately to optimize the signal detection sensitivity over a large depth range. Considering these issues, we designed and implemented the units as shown in Fig. 3.

In determining the beam path, our main goal was to make the laser beam illuminate the target tissue as perpendicular as possible to the axis of the endoscope and to ensure that the laser beam overlapped the acoustic axis of the US transducer that detects the PA waves reflected by the sapphire window [Fig. 3(a)]. To achieve this objective, we conceived a laser-beam guiding method that uses an angle-polished fiber in combination with a small dielectric mirror that is attached on the stainless steel frame along with the sapphire window as shown in Fig. 3(b). Figure 3(c) shows the entire scanning mirror encapsulated in a stainless steel tube (outer diameter: 2.1 mm).

As shown in Fig. 3(a), the laser beam is fired toward the dielectric mirror from the multimode optical fiber (core diameter: 365-μm, $n = 1.463$ at 532 nm) and then reflected by the dielectric mirror. Because the optical fiber tip was polished at a 30-deg angle [Fig. 3(a)], the exiting laser beam is deflected by ~43 deg (for the chief ray) as shown in Fig. 3(d); an example of the beam shape exiting the optical fiber is presented in Fig. 3(e). However, by adding a reflection plane (the dielectric mirror) with a tilt angle of ~15 deg to the endoscope axis [Fig. 3(a)], we could increase the laser-beam illumination angle to ~66 deg after it exited the sapphire window ($n = 1.768$). Figure 3(f) shows the final laser-beam firing direction and the acoustic axis of the transducer, from which one can see a mismatch, whose effect will be discussed later. The laser-beam firing method using an angle-polished optical fiber was first introduced by Karpiouk et al. in their intravascular imaging catheter.[20] However, we added the dielectric mirror to increase the incident angle to the target tissue.

To more accurately analyze the laser-beam profile, we utilized a beam profiler (OPHIR Beam Gauge). As presented in Fig. 3(g), the measured beam profile showed a broad illumination pattern, and the beam area with the intensity larger than 90% of the peak value at the central zone was ~0.64-mm^2 when it passed through the imaging window; ~7.3% of the total energy was concentrated in this area. Thus, the set 0.25-mJ pulse energy yielded an optical fluence of lower than 3 mJ/cm^2 (i.e., 15% of the American National Standards Institute safety limit[38] for allowable skin laser fluence). The image resolution of this endoscopic system is determined by

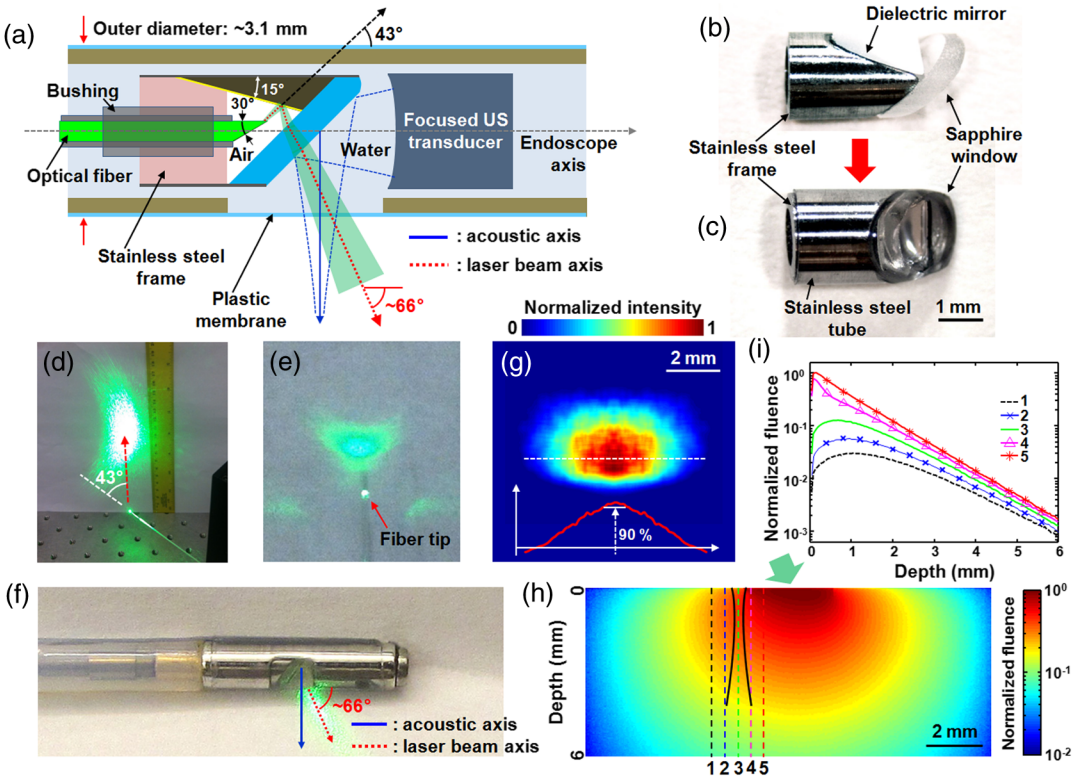

Fig. 3 (a) Schematic showing the configuration of optical and acoustic components at the distal end. (b) Photo of the dielectric mirror and sapphire window attached on a stainless steel frame. (c) Photo of the entire scanning mirror encapsulated in a stainless steel tube [rotated by ~90 deg from (b)]. (d) Photo of laser beam projected horizontally to a screen with a deflection angle of 43 deg. (e) Top view of the optical fiber tip and beam profile projected to a screen. (f) Photo showing the laser beam firing direction and acoustic axis of the endoscope. (g) Approximate beam profile of the laser beam exiting the endoscope. To remove the intensity fluctuations caused by speckle, we averaged the original raw data image from the beam profiler. (h) Monte Carlo simulated two-dimensional fluence distribution in the plane including the laser-beam axis and the acoustic axis. (i) Fluence variations along the dotted lines shown in (h). Line #3 indicates the fluence distribution along the acoustic axis.

the acoustic parameters of the focused US transducer because no light focusing optics are coupled with the optical fiber. In designing the endoscope, we targeted a working distance of ~2-mm from the endoscope's surface to image human upper GI tracts with Barrett's esophagus in direct contact mode; Barrett's esophagus is a representative esophageal disease developed in the epithelial layer of the lower esophagus and regarded as a precursor of esophageal cancer.

Using the beam profile data [Fig. 3(g)] and considering the laser-beam incident and diverging angles, we performed a Monte Carlo simulation[39] to estimate the optical fluence distribution in the target tissue near the acoustic axis. For the simulation, we assumed a semi-infinite medium for the target tissue with a planar and index-matched boundary (relative refractive index $n_{\text{rel}} = 1$) and optical properties of absorption coefficient $\mu_a = 1.5\ \text{cm}^{-1}$, scattering coefficient $\mu_s = 200\ \text{cm}^{-1}$, and scattering anisotropy $g = 0.908$; these optical properties were of human mucosa tissue reported by Bashkatov et al.[40] As shown in the simulation result [Fig. 3(h)], the irradiated laser beams [Fig. 3(g)] quickly diffuse omni-directionally after propagating one transport mean free path (~0.5-mm). The fluence distribution along the acoustic axis is plotted in Fig. 3(i). Even though there is a mismatch between the laser-beam firing direction and the acoustic axis, the endoscope can acquire PA A-line signals over a large depth.

2.3 *Fabrication of the Focused Ultrasonic Transducer*

For this endoscope, we implemented a self-focused US transducer (1.7-mm aperture, $f = 5$-mm) using lithium niobate ($LiNbO_3$) for the piezoelectric material. Figures 4(a) and 4(b) show a schematic and a photo of the implemented transducer. The transducer's structure and fabrication process were similar to those of the transducer previously utilized for the micromotor-based endoscopic probe.[15–18] However, we achieved the focusing by applying a press-focusing technique[41] that forms the piezo-element's concave shape through a cracking process created by pressure applied to the planar surface of the piezo-element. The pressure was typically applied by a steel bearing ball with the same radius as the desired focal distance (i.e., 5-mm for this case). Compared with the previous lens-based focusing technique that affixed a plastic acoustic lens to the surface of a flat transducer,[16,18] the press-focusing technique enabled the fabrication of a focused US transducer with a higher sensitivity than a lens-based counterpart (i.e., without the acoustic attenuation caused by the plastic lens) and also yielded a higher success rate in the focused transducer fabrication process. We measured the insertion loss of the transducer to be 27.6 dB (water attenuation compensated), which was higher than that of the previous transducer[16] because of the higher electrical

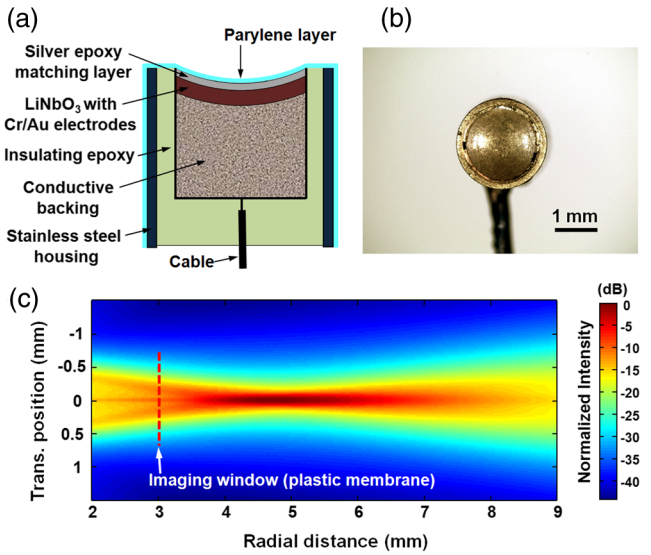

Fig. 4 Schematic (a) and photo (b) of the focused US transducer implemented by applying the press-focusing technique. (c) Simulated transmission (i.e., one-way) acoustic intensity map of the focused transducer.

impedance mismatch caused by the reduced element area (output impedance: ~300 Ω).

In Fig. 4(c), we also present the transmission (i.e., one-way) acoustic intensity map of the focused transducer. We acquired the intensity map using an acoustic modeling software package (Field II),[42,43] assuming the immersion medium to be water. As the US transducer is spherically focused, its transverse resolution varies with depth from the transducer surface (radial distance); the highest resolution zone of the transducer is located ~2-mm from the imaging window (plastic membrane). In general, a focused US transducer provides excellent transverse resolution in the focal zone, but out of the focal zones, its transverse resolution degrades more quickly than that of an unfocused transducer. Nevertheless, we utilized such a focused type US transducer to resolve blood vessels distributed in the human esophageal wall. We also chose lithium niobate single crystal as the piezo-electric material because it consistently shows high performance for the press-focusing technique.

2.4 *Affixing the Electric Signal Wire of the Ultrasonic Transducer*

Unlike in our previous micromotor-based endoscopic probes,[15–18] the US sensor in this PAE system is placed near the tip of the probe, and the flexible shaft and the scanning mirror are closer to the proximal part, occupying most of the inner space of the 2.5-m long plastic catheter section. To route the signal wire of the US transducer, we applied a static mounting method, which affixes the signal wire on the outer surface of the PTFE plastic catheter, using two thin PET plastic tubes (~25-μm thickness), as illustrated in Fig. 5(a). We had applied this static mounting method in our previous endoscopic systems[15–18] and learned that it minimizes the interference noise that is typically caused by the nearby pulsed laser system. Figures 5(b) to 5(h) show the detailed procedure for affixing the signal wire.

In this catheter endoscope, we utilized a 0.44-mm diameter coaxial cable (50 Ω, 40232-1-600-S-00000, Hitachi Cable Manchester, Purchase) for the signal wire of the transducer and a 3.2-mm outer diameter PTFE plastic catheter (wall thickness: 0.80-mm) for the sheath of the flexible shaft. To create a route for the signal wire without exceeding the 3.2-mm probe diameter, we first milled one side of the stainless steel housing as shown in Fig. 5(b) and also removed ~0.4-mm from one side of the PTFE plastic catheter, as shown in Fig. 5(c). We then carefully aligned the signal wire along the milled groove [Fig. 5(d)] and the flat surface [Fig. 5(e)]. Finally, we secured the wire

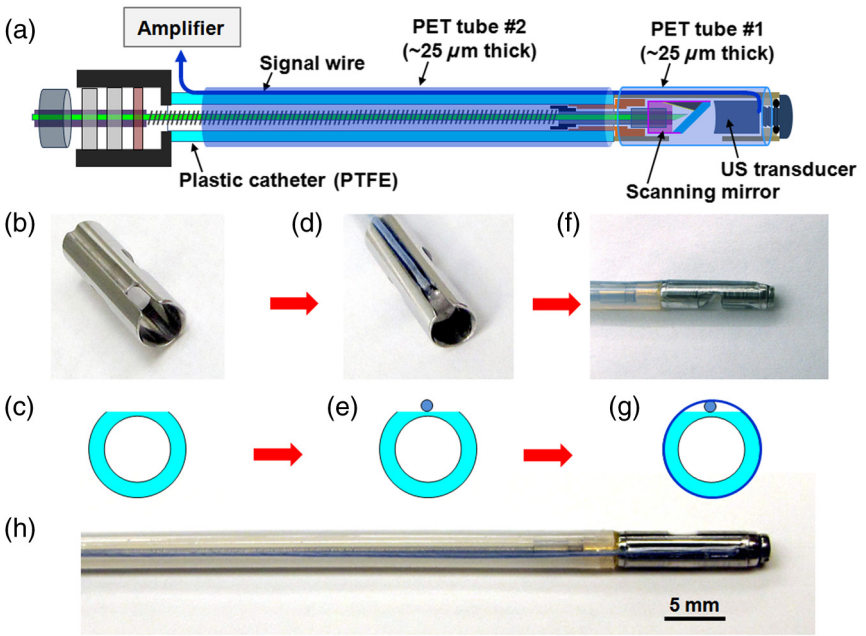

Fig. 5 (a) Illustration of the affixed US transducer's signal wire. (b–g) Procedure for affixing the signal wire at the stainless steel housing (b, d, f) and plastic catheter (c, e, g). (h) Photo of the catheter probe after affixing the signal wire.

using two medical-grade PET tubes #1 (103-0380, Advanced Polymers) and #2 (103-0147, Advanced Polymers) over the 16-mm long rigid distal section [Fig. 5(f)] and the 2.5-m long flexible body section [Fig. 5(g)]. PET tube #1 is the same as that used to form the imaging window discussed in Sec. 2.1; so, it is optically and acoustically transparent and seals the inner space of the probe. Figure 5(h) is a photograph of the secured signal wire, and the proximal situation of the wire is shown in Fig. 2. Owing to the passage of the signal wire along one side of the imaging window, the endoscope's angular field-of-view (FOV) was limited to ~160 deg.

Enclosing the signal wire using the PET tubes also provides a simple solution for sterilization of the endoscope. As the PET tubes (#1 and #2) are very strong for their wall thickness (~25-μm), they safely isolate the inner components from physical contact with the target tissue, and their surface can be easily sterilized with 70% ethanol or ethylene oxide. Also, the thin-wall PET tubes can be easily removed using an ordinary surgical blade and replaced with new ones whenever necessary. Although the replacement work cannot be done quickly in clinical settings, it will definitely benefit hygiene and safety.

2.5 *Providing an Acoustic Matching Medium for the Inner Cavity of the Endoscope*

As mentioned previously, providing an appropriate acoustic matching medium for the inner cavity of this endoscopic probe is also important to efficiently transmit generated PA waves to the US transducer. In this study, similar to our previous endoscopic systems,[15–18] we utilized deionized water as the matching medium, which exhibits both high optical transparency and low acoustic attenuation for high-frequency acoustic waves. However, it gradually corrodes the metallic components and degrades the glued points. Thus, to counteract these problems, we added water injection and drainage ports to the endoscopic system. Before each endoscopic experiment, we fill the inner space of the endoscope with deionized water and drain it after use. Figure 6 depicts the water injection procedure and related system components.

For water injection, we open the sealing screw at the distal end of the probe and immerse the water injection port into a tank of deionized water, as shown in Fig. 6(a). Then, we connect a water drainage hose to a vacuum pump (installed in the fume hood in an ordinary laboratory), which sucks up the water. Once the vacuum pump is switched on, the water starts to fill the inner cavity of the distal end by flowing through a narrow channel formed on one side of the US transducer. It then gradually moves to the flexible catheter section via the narrow gap between the stainless steel tubular shaft and the bronze sleeve bearing. It finally exits through the water drainage hose located at the proximal actuation unit (Fig. 2). The blue arrows in the diagram show the water flow route. Once the inner cavity is filled with water, the water injection port is blocked using the sealing screw, as presented in Figs. 6(b) and 6(c). If, on the visual inspection under a ~20× microscope, bubbles are seen inside the cavity, the same procedure is repeated until no bubbles appear.

Although we inject deionized water, it still has to be drained after the experiment because it gradually becomes ionized, which would corrode the metallic components. For drainage, we open the water injection port and connect the water drainage hose to the same vacuum system. When the water has been drained, we flush the inner cavity several times using 95% ethanol, following the same injection method, then maintain the vacuum connection for several hours to completely remove the ethanol.

3 Quantifying the Imaging Performance and Testing Intra-Instrument Channel Workability

After building the system, we tested its mechanical performance and also quantified its image resolution. With the capacity of the employed step motor, the PAE system could reach a maximum B-scan speed of 5 Hz, corresponding to an A-line acquisition rate of 2 kHz; higher scanning speeds were limited by the mechanical friction caused by the long length of the flexible shaft. To analyze the endoscopic probe's spatial resolution and scanning stability, we imaged a ~20-μm diameter tungsten wire in a water tank. We placed the target at the focal position of

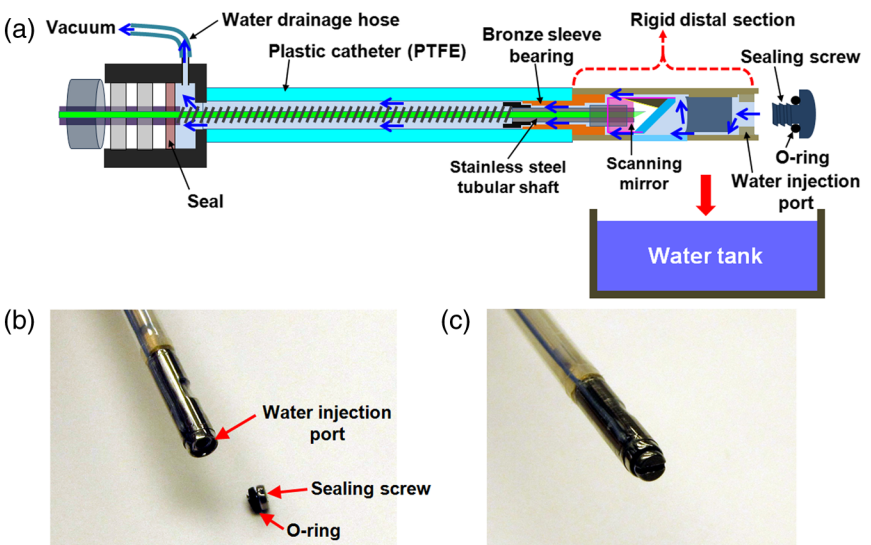

Fig. 6 (a) Illustration showing a water injection method for providing acoustic matching in the inner cavity of the endoscope. Photos of the inlet with the sealing screw opened (b) and closed (c).

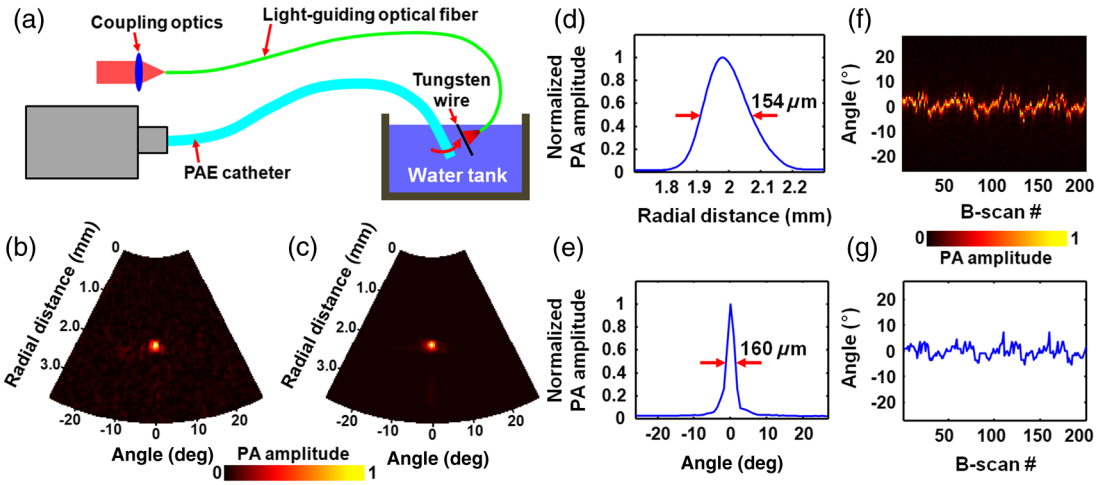

Fig. 7 (a) Experimental setup for quantifying the spatial resolution of the endoscope using a tungsten wire in clear water. (b) Typical PAE B-scan image of the 20-μm diameter tungsten wire [only 54 deg angular field-of-view (FOV) is presented]. (c) Averaged image of the tungsten wire from 200 B-scan images. Radial (d) and transverse (e) line spread functions of the tungsten wire shown in (c). (f) Radial-maximum amplitude projection image of the tungsten wire processed from 200 B-scan images. (g) Center position graph of the tungsten wire extracted from (f).

the endoscope (2-mm from the endoscope surface) and recorded 200 B-scan images. In this phantom experiment, however, we delivered laser pulses to the target using a different light-guiding optical fiber because the experiment was performed in a clear medium that did not scatter the obliquely fired laser beam to the scanning plane of the transducer. So, as shown in Fig. 7(A), we connected the light-guiding optical fiber to the coupling optics of the endoscope and performed the B-scan imaging by illuminating the wire target from one side, while keeping all other settings the same. Although we performed this resolution experiment by exciting the target using a different optical fiber, its results are valid because the spatial resolution of this acoustic-resolution PA endoscope is nearly solely determined by the focused US transducer, that is, not by the optical illumination.

Figure 7(b) shows a typical PA B-scan image acquired from the tungsten wire; because PA A-line raw data include negative values, that is, they are bipolar, we applied the Hilbert transformation to extract the envelope of the signal. To more accurately quantify the resolution, we averaged the 200 B-scan images pixel by pixel. From the averaged image [Fig. 7(c)], we acquired the radial and transverse line spread functions (LSFs) presented in Figs. 7(d) and 7(e), respectively. By analyzing the full widths at half maximum (FWHMs) of the LSFs, we determined the radial and transverse resolutions to be ~150- and ~160-μm, respectively. These experimental resolutions were worse than the theoretically estimated resolution values of 43-μm (radial) and 156-μm (transverse); the large discrepancy in the radial resolution was caused by the electric impedance mismatch between the transducer and the amplifier that resulted in a narrowed effective bandwidth for the transducer.

Using the 200 B-scan images, we also analyzed the mechanical jitter (or scanning stability) of the scanning mirror. As presented in Fig. 7(f), which was produced by applying a typical radial maximum amplitude projection process to the 200 B-scan images, the recorded positions of the wire target were not constant and showed a fluctuation in the lateral direction (i.e., in angle) caused by the nonuniform rotation of the scanning mirror. We extracted the center positions of the tungsten wire in angle value [Fig. 7(g)] and determined the root-mean-square (rms) lateral fluctuation of the scanning mirror to be ~2.2 deg.

While the radial resolution of the focused US transducer shows a relatively constant value, its transverse resolution shows a large variation according to depth. To investigate the depth dependence, we imaged two hypodermic needles embedded in an Intralipid-gelatin-based tissue mimicking phantom. Figures 8(a) and 8(b) show the structure and photo of the phantom, respectively. In creating the phantom, we utilized a 33 gauge (Object 1, ~210-μm diameter) and a 30 gauge (Object 2, ~310-μm diameter) needle as light absorbing objects and fixed them at ~2.0- and 4.5-mm depths from the surface of the phantom using a metal frame [Fig. 8(b)]. We added 20% Intralipid (Fresenius Kabi, purchased from VWR International, #68100-276) to a gelatin–water solution to mimic the reduced scattering coefficient of typical mucosa tissue (~18 cm^{-1}).[40] The gelatin was purchased from Sigma–Aldrich (#G2500-1kG; gel strength 300, Type A), and the Intralipid–gelatin–water phantom was made according to the recipe in Ref. 44. In this experiment, we utilized relatively large diameter targets compared with the previous tungsten wire imaging experiment to acquire PA signals with adequate signal-to-noise ratios; as the matrix medium is turbid, the optical fluence near the objects is much weaker than that in the clear medium. Also, the diameters of the two needles were selected according to the theoretical resolution values, although the diameter of Object 1 was ~35% larger than the theoretical resolution value at the position.

Figure 8(c) shows a representative B-scan image acquired from the phantom. In this experiment, unlike the previous tungsten wire imaging experiment conducted in a clear medium [Fig. 7(a)], laser pulses were delivered through the optical fiber enclosed in the catheter endoscope because the targets were embedded in the scattering medium. As shown in the image, we could detect PA signals from the two objects with adequate signal-to-noise ratios. From the image, we plotted the transverse signal variations for the two needles in Figs. 8(d)

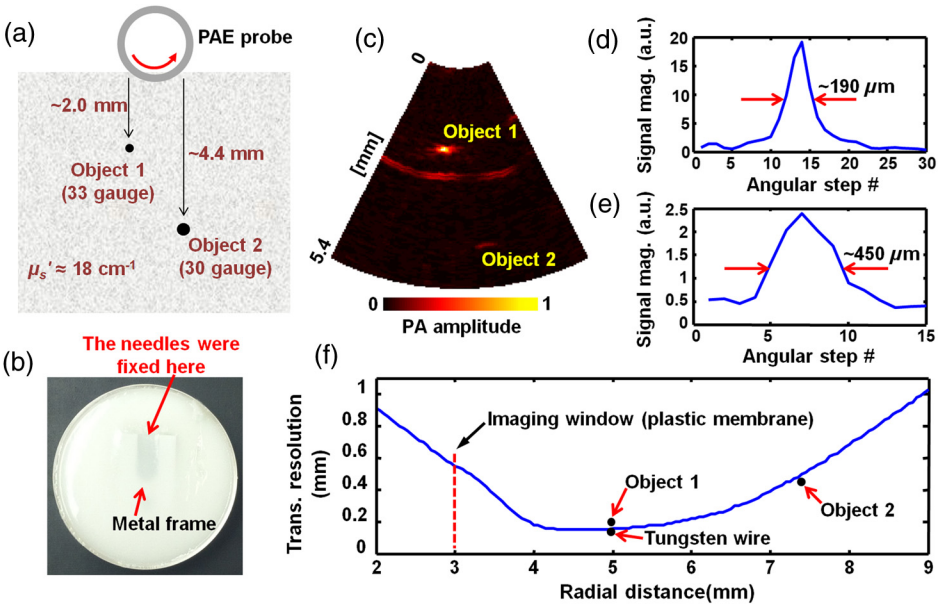

Fig. 8 (a) Structure of the Intralipid-gelatin-based tissue mimicking phantom including two metal objects (side view). Objects 1 and 2 are 33 gauge (~210-μm diameter) and 30 gauge (~310-μm diameter) hypodermic needles, respectively. (b) Photo of the phantom (top view). (c) Typical PAE B-scan image of the two needles (only 54 deg angular FOV is presented). (d and e) Transverse signal variations of the two needles analyzed from (c). (f) Transverse resolutions versus radial distance. The solid line was estimated from the simulation result [Fig. 4(c)], and the dots were determined by the experiments.

and 8(e). Based on the FWHMs of the two plots, we roughly estimated the transverse resolutions to be ~190- and ~450-μm at the two distances, respectively. Because Object 1 has a round surface and is located in the focal zone, the FWHM of the curve [Fig. 8(d)] appeared to be even smaller than the actual diameter; one can see that only the areas of the two-needle surfaces that were closer to the US transducer were visualized by the endoscope (especially Object 2).

To compare the experimental results with the theoretical values, we present in Fig. 8(f) the theoretical resolution from Fig. 4(c). As shown, the resolution values estimated by the two needles (Objects 1 and 2) are close to the theoretical values. However, the tungsten wire's resolution value showed a slightly closer agreement with the theoretical value. As the tungsten wire's resolution value was measured in water immersion, like the assumption of the simulation, the high agreement implies that the fabrication of the transducer was nearly ideal. Therefore, we can reasonably estimate the transverse resolution values at other distances from the theoretical curve.

After quantifying the resolution, we also tested the endoscope's intra-instrument channel workability. Because the endoscope's outer diameter is ~3.2-mm, we utilized the 3.7-mm diameter instrument channel of a clinical video endoscope (13911 NKS, Karl Storz, Tuttlingen, Germany). As shown in Fig. 9(a) and Video 1, we were able to easily insert the catheter endoscope into the entry port of the instrument channel and were also able to perform angulation smoothly along with the video endoscope. Figure 9(b) shows the tip of the catheter endoscope projected from the exit port of the video endoscope, and Fig. 9(c) represents a magnified view of the catheter endoscope emitting green laser light (532-nm). After performing a course of angulation and mechanical scanning, we were able to retract the probe uneventfully (Video 2).

4 In Vivo Animal Imaging Experiment

To demonstrate the endoscope's *in vivo* imaging capability, we imaged the upper esophagus of a New Zealand white rabbit (~4 kg, female, 7 months old, Harlan Laboratories, Indianapolis). Because the typical diameter (~5-mm) of a rabbit's esophagus is much narrower than that of the video endoscope (~13-mm), we imaged the rabbit esophagus using only the PAE probe.

For the experiment, the rabbit was fasted, beginning ~12 h before the experiments, to reduce the likelihood of ingesta in the stomach and esophagus. The rabbits were anesthetized with 35 to 50 mg/kg of ketamine and 5 to 10 mg/kg of xylazine via intramuscular injection. While anesthetized, the rabbit was intubated for maintenance of gas anesthesia (1.5% to 3.0% isoflurane). An endotracheal tube cuff was inflated to prevent aspiration of water into the lung. The rabbit was placed on an inclined stage (~10 deg) in a supine position. Just before the probe insertion, we filled the esophagus with water using an enteral feeding syringe connected to a rubber feeding tube (8 to 12 F or 2.7- to 4.0-mm). The water provided the necessary acoustic coupling and functioned as a lubricant during the imaging procedure. After filling the stomach and esophagus with water, we inserted the endoscopic probe through the mouth and advanced it ~25-cm, to the point at which the probe could no longer be gently advanced. Then, we performed pullback volumetric scans over a ~6 cm range during constant pullback translation of the probe by a motorized translation stage at a speed of ~150-μm/s. For this animal experiment, we set the gain of a signal amplifier at 40 dB and acquired about 2000 B-scan slices with a longitudinal spacing of ~30-μm. Throughout the experiment, the rabbit's anesthesia level and vital signs were continuously monitored. After the experiment, the rabbit was euthanized by an overdose of sodium

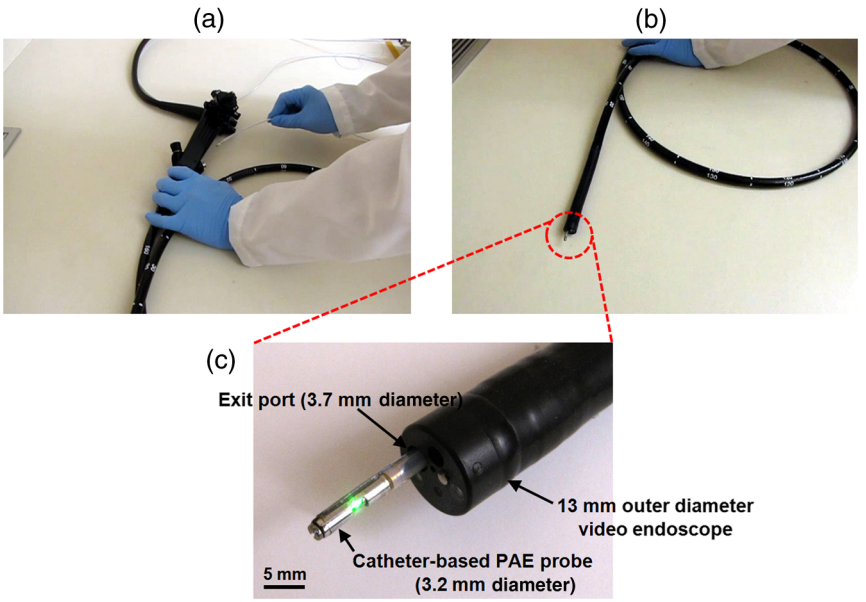

Fig. 9 Photos of the catheter-based PAE probe positioned fully within (a) and projecting from (b) the 3.7-mm instrument channel of a clinical video endoscope (Video 1, QuickTime, 9.86 MB [URL: http://dx.doi.org/10.1117/1.JBO.19.6.066001.1]; Video 2, QuickTime, 3.43 MB) [URL: http://dx.doi.org/10.1117/1.JBO.19.6.066001.2]. (c) Magnified view of (b).

pentobarbital (150 mg/kg) injected in the marginal ear vein. All procedures in the experiment followed the protocol approved by the Institutional Animal Care and Use Committee at Washington University in St. Louis.

In Fig. 10, we present several postexperiment-processed PA B-scan images, covering a 160-deg angular FOV and 5.4-mm imaging depth, plotted on a linear [Figs. 10(a) to 10(c)] and a logarithmic [Figs. 10(d) to 10(f)] color scale. A partial pull-back movie showing 800 B-scan slices is available in Video 3.

As shown in the B-scan images [Figs. 10(d) to 10(f)], the PAE system provided cross-sectional images of the esophagus and its neighboring anatomic structures. From our previous animal imaging experiments,[17] we learned that the typical wall thickness of a rabbit esophagus is just ~400- to 600-μm [see the histologic image, Fig. 2(i), in Ref. 17]. The neighboring space of the upper esophagus is occupied by the thymus and fat tissues, which are not very light absorptive [see the anatomic image, Supplementary Fig. 7(a), in Ref. 17]. In Figs. 10(d) to 10(f),

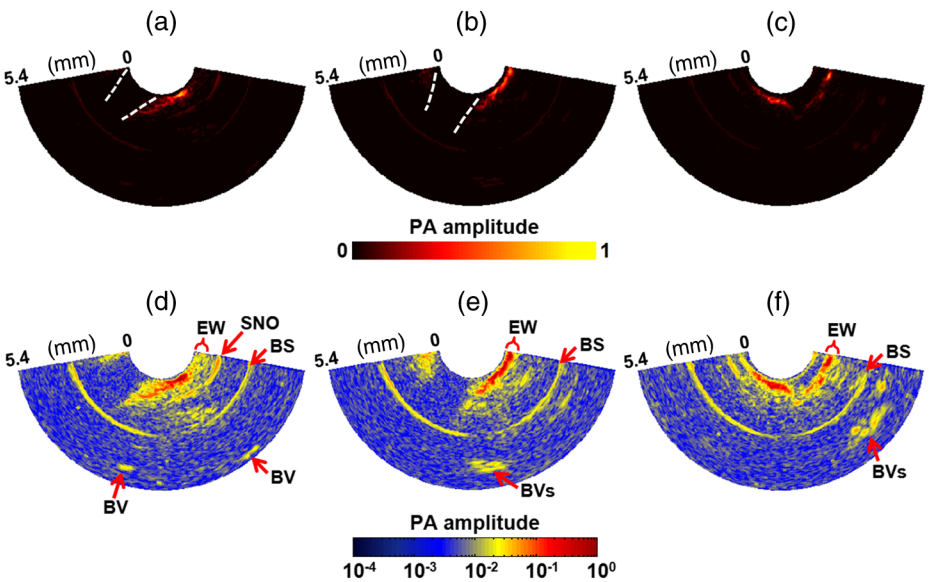

Fig. 10 Representative PAE B-scan images of a rabbit esophagus acquired *in vivo* shown on (a)–(c) a linear and (d)–(f) a logarithmic color scale (Video 3, QuickTime, 4.60 MB) [URL: http://dx.doi.org/10.1117/1.JBO.19.6.066001.3.3]. The images cover a ~14-mm diameter (i.e., ~5.4-mm radial imaging depth) and ~160 deg angular FOV. The left-hand side and lower portion of each image correspond to the left and the dorsal side of the animal, respectively. BS, bounceback signals; BV, blood vessel; EW, esophageal wall; and SNO, surface of a neighboring organ.

we provide several landmarks, such as the esophageal wall, a surface of a neighboring organ [Fig. 10(d)], and multiple blood vessels (the arrows) distributed in the mediastinum. As the endoscope was designed to work in direct contact mode, we could not detect PA signals when the probe's distance to the esophageal surface increased beyond approximately more than 1.5-mm [see the dotted lines in Figs. 10(a) and 10(b)]; this dead zone was due to the misalignment between the light illumination and the acoustic detection (Fig. 3). Also, blood vessels in the esophageal wall were not clearly resolved because the acoustic focus was located ~2-mm away from the endoscope surface. If the surface of the esophageal wall, which has a thickness of <1-mm, is located at a distance beyond ~1.5-mm, the corresponding scanning area becomes a dead zone. Thus, all the esophageal walls imaged in this experiment were located within the 1.5-mm distance, i.e., out of optimal focus.

In the presented B-scan images, one can also see arc-shape lines at ~3-mm depth; similar lines also appeared in our previous PAE images.[17] From a couple of tests, we found that it is a bounceback signal (i.e., acoustic reflection) of the PA waves generated at the US transducer surface. Because the tip of the angle-polished optical fiber was cracked a little bit during the polishing and assembling process, whenever laser pulses are fired, stray light is generated, and some of them impinge on the transducer surface, which then creates PA waves. At the same time, PA waves are also generated at the surface as well as the deep regions of the target tissue. Consequently, some portions of the PA waves generated from the two sources started to propagate in opposite directions, and they reached the membrane and transducer surface, respectively, after ~2-μs, which corresponds to the traveling time of acoustic waves for the distance (i.e., ~3-mm) from the plastic membrane to the transducer surface via the scanning mirror. The PA waves originating from the tissue are the true signals that we want to record. However, the PA waves originating from the transducer surface are also recorded after another 2-μs, which corresponds to the return travel time, i.e., from the membrane to the transducer. In the case of the tungsten wire imaging [Fig. 7(a)], such an arc-shape line was not generated because it was acquired using external illumination, i.e., not using the endoscope's optical fiber.

With this *in vivo* imaging data, we also analyzed the scanning stability of the scanning mirror using the PA signals generated by the stainless steel bridge section [Fig. 1(c)]; usually metallic objects generate strong PA signals because they are highly light absorbing. The result showed a greater fluctuation (8.6 deg rms) than the tungsten wire imaging experiment because the endoscope performed mechanical scanning while bent. In addition, we found that the nonuniformity of the rotation of the flexible shaft showed periodic changes in accordance with the respiratory motion of the animal. Due to this nonuniform rotation and the respiratory motion, we were unable to produce a radial maximum amplitude projection or a volumetric image.

5 Discussion

In this study, we implemented a new catheter-based PAE system and demonstrated its intra-instrument channel workability with a clinical video endoscope and *in vivo* imaging ability through an animal experiment. Compared with our previous micromotor-based endoscopes,[15–18] this PAE probe has a more flexible and simplified distal structure with a smaller number of mechanical components, which promotes its clinical applicability. To transmit electric signals from the US transducer while minimizing interference noise, we employed a previously used[15–18] static mounting method for the signal wire [Fig. 5(a)]. However, we delivered the laser beam via a rotary junction formed at the proximal unit of the endoscope [Fig. 1(a)]. Importantly, by using a flexible shaft instead of a micromotor [Fig. 1(a)], we were able to achieve a rigid distal section length of only 16-mm, two times shorter than the previous micromotor-based endoscope[18] and to enable the catheter section to pass freely through the 3.7-mm diameter entry port of a video endoscope. Although other PA endoscopic systems[20–24] have been implemented with a similar proximal actuation mechanism, their imaging probes are not sheathed in a plastic tube and/or their *in vivo* imaging capabilities have not been demonstrated. We believe that the presented PAE system is the first PA endoscopic system that has been implemented in a fully encapsulated form and sufficiently miniaturized to be usable for endoscopic imaging via the standard instrument channel of a clinical video endoscope.

With the prototype imaging system, we achieved a B-scan imaging speed of ~5 Hz (corresponding to an A-line acquisition rate of ~2 kHz and ~400 A-lines/B-scan), which is slightly faster than that (~4 Hz) of our previous micromotor-based endoscopic probes.[15–18] However, we were not able to produce a volumetric image because of the nonuniform rotation of the scanning mirror; such nonuniform rotation was not a serious issue in the micromotor-based endoscopic probes. The slow scanning speed could be further improved by simply using a higher capacity step motor. However, first the mechanical friction between the shaft and the plastic sheath needs to be reduced to minimize the mechanical stress (torsion) caused by the angular phase delay between the proximal and distal ends of the flexible shaft. As we mentioned in the *in vivo* experimental results (Fig. 10), the mechanical friction and the corresponding rotational nonuniformity increased as the catheter bent more because of the large thickness of the employed multimode optical fiber. An oil-based matching medium could be helpful in reducing the friction. However, high optical transparency and low acoustic attenuation are needed for a PA endoscope. If these requirements are satisfied, such an oil-based medium would also beneficially eliminate the acoustic matching medium injection and drainage procedure (Fig. 6) because the medium could be retained in the catheter perpetually.

With the proposed optical design (Fig. 3), we detected PA signals over a large imaging depth in the *in vivo* rabbit esophagus imaging experiment, although the laser-beam firing direction did not coincide with the acoustic axis. However, because of the misalignment, we could not detect PA signals when the probe's distance to the target surface increased beyond ~1.5-mm [Figs. 10(a) and 10(b)]; the endoscope must work in a direct contact to the optical scattering tissue. Also, PA images could be distorted when the US transducer's out-of-plane signals are stronger than the real in-plane signals. Thus, the next generation PAE system should improve the light-guiding optics in the scanning mirror to overlap the optical illumination and the acoustic detection, enabling it to cover the entire radial imaging depth. It was difficult to realize this in the current version because the diameter of the beam exiting the multimode optical fiber was very large compared to the available space in the scanning mirror unit. An optical fiber with a narrower diameter, such as a single-mode fiber, would be conducive to aligning the optical illumination and the acoustic detection. Another

important challenge is to encase the entire probe in a single length of a plastic catheter to increase flexibility. As the presented catheter endoscope system was specifically developed for intrainstrument channel use, this encasing method will make the catheter endoscope more durable and thereby safer.

In this study, we achieved a 3.2-mm probe diameter, allowing insertion of the probe in a 3.7-mm diameter instrument channel of a standard GI video endoscope; the main factor that determined the current probe diameter was the space required to accommodate the large diameter scanning mirror and the spherically focused US transducer. However, achieving a smaller probe diameter, such as 2.4-mm, will make related PAE imaging probes compatible with even narrower instrument channels, such as 2.8-mm. In recent years, as a method for pursuing higher miniaturization, an optical ultrasound detection[22] and bundle fiber-based optical scanning[45] mechanism has been proposed by other groups. However, the optical signal detection method currently suffers from instability in the probe fabrication as well as the signal detection, and the image FOV of the bundle fiber-based optical scanning endoscope is narrow unless it performs additional scanning. Nevertheless, those methods could be potentially good options because they can make related probes' design simpler and the footprint smaller.

6 Conclusions

We have successfully implemented a prototype PAE system that has a 3.2-mm diameter and 2.5-m long catheter section and demonstrated its endoscopic imaging ability through an *in vivo* rabbit esophagus imaging experiment. The endoscopic system can produce PA images with a B-scan frame rate of ~5 Hz and an A-line acquisition rate of 2 kHz. Most notably, the 3.2-mm diameter catheter is small enough to pass through the 3.7-mm diameter standard instrument channel of a clinical video endoscope. With this endoscope, we will progress to imaging human subjects with Barrett's esophagus.

Acknowledgments

The authors thank Professor James Ballard for his attentive reading of the paper and Dr. Konstantin Maslov for useful discussions on the system design. The authors also thank Lisa Andrews-Kaminsky and Jenny Kalishman for helping with the animal experiment. This work was sponsored in part by National Institutes of Health Grants Nos. R01 CA157277, DP1 EB016986 (NIH Director's Pioneer Award), R01 EB016963, and R01 CA159959. L.W. has a financial interest in Microphotoacoustics, Inc. and Endra, Inc., which, however, did not support this work.

References

1. A. A. Oraevsky and A. A. Karabutov, "Optoacoustictomography," in *Biomedical Photonics Handbook*, T. Vo-Dinh, Ed., CRC Press, New York (2003).
2. L. V. Wang, "Multiscale photoacoustic microscopy and computed tomography," *Nat. Photonics* **3**(9), 503–509 (2009).
3. S. Y. Emelianov, P.-C. Li, and M. O'Donnell, "Photoacoustics for molecular imaging and therapy," *Phys. Today* **62**(5),34–39 (2009).
4. V. Ntziachristos, "Going deeper than microscopy: the optical imaging frontier in biology," *Nat. Methods* **7**(8), 603–614 (2010).
5. P. Beard, "Biomedical photoacoustic imaging," *Interface Focus* **1**(4), 602–631 (2011).
6. L. V. Wang and S. Hu, "Photoacoustic tomography: in vivo imaging from organelles to organs," *Science* **335**(6075), 1458–1462 (2012).
7. J. Yao et al., "Label-free oxygen-metabolic photoacoustic microscopy in vivo," *J. Biomed. Opt.* **16**(7), 076003 (2011).
8. L. Song, K. Maslov, and L. V. Wang, "Section-illumination photoacoustic microscopy for dynamic 3D imaging of microcirculation in vivo," *Opt. Let.* **35**(9), 1482–1484 (2010).
9. S. Hu, K. Maslov, and L. V. Wang, "Second-generation optical-resolution photoacoustic microscopy with improved sensitivity and speed," *Opt. Lett.* **36**(7), 1134–1136 (2011).
10. M. Nasiriavanaki et al., "High-resolution photoacoustic tomography of resting-state functional connectivity in the mouse brain," *Proc. Natl. Acad. Sci. U. S. A.* **111**(1), 21–26 (2014).
11. J. Yao et al., "Wide-field fast-scanning photoacoustic microscopy based on a water-immersible MEMS scanning mirror," *J. Biomed. Opt.* **17** (8),080505 (2012).
12. J. Yao et al., "Absolute photoacoustic thermometry in deep tissue," *Opt. Lett.* **38**(24), 5228–5231 (2013).
13. M. R. Chatni et al., "Functional photoacoustic microscopy of pH," *J. Biomed. Opt.* **16**(10), 100503 (2011).
14. Y. Wang and L. V. Wang, "Forster resonance energy transfer photoacoustic microscopy," *J. Biomed. Opt.* **17**(8), 086007 (2012).
15. J. M. Yang et al., "Photoacoustic endoscopy," *Opt. Lett.* **34**(10), 1591–1593 (2009).
16. J. M. Yang et al., "Volumetric photoacoustic endoscopy of upper gastrointestinal tract: ultrasonic transducer technology development," *Proc. SPIE* **7899**, 78990D (2011).
17. J. M. Yang et al., "Simultaneous functional photoacoustic and ultrasonic endoscopy of internal organs in vivo," *Nat. Med.* **18**(8), 1297–1302 (2012).
18. J. M. Yang et al., "A 2.5-mm diameter probe for photoacoustic and ultrasonic endoscopy," *Opt. Express* **20**(21), 23944–23953 (2012).
19. B. Wang et al., "Intravascular photoacoustic imaging," *IEEE J. Sel. Top. Quantum Electron.* **16**(3), 588–599 (2010).
20. A. B. Karpiouk, B. Wang, and S. Y. Emelianov, "Development of a catheter for combined intravascular ultrasound and photoacoustic imaging," *Rev. Sci. Instrum.* **81**(1), 014901 (2010).
21. K. Jansen et al., "Intravascular photoacoustic imaging of human coronary atherosclerosis," *Opt. Lett.* **36**(5), 597–599 (2011).
22. E. Z. Zhang and P. C. Beard, "A miniature all-optical photoacoustic imaging probe," *Proc. SPIE* **7899**, 78991F (2011).
23. B. Wang et al., "Intravascular photoacoustic imaging of lipid in atherosclerotic plaques in the presence of luminal blood," *Opt. Lett.* **37**(7), 1244–1246 (2012).
24. A. B. Karpiouk et al., "Feasibility of in vivo intravascular photoacoustic imaging using integrated ultrasound and photoacoustic imaging catheter," *J. Biomed. Opt.* **17**(9), 096008 (2012).
25. X. Wang et al., "Photoacoustic tomography: a potential new tool for prostate cancer," *Biomed. Opt. Express* **1**(4), 1117–1126 (2010).
26. Y. Yang et al., "Integrated optical coherence tomography, ultrasound and photoacoustic imaging for ovarian tissue characterization," *Biomed. Opt. Express* **2**(9), 2551–2561 (2011).
27. J. Menzel and W. Domschke, "Gastrointestinal miniprobe sonography: the current status," *Am. J. Gastroenterol.* **95**(3), 605–616 (2000).
28. C. Dietrich, Ed., *Endoscopic Ultrasound: An Introductory Manual and Atlas*, Thieme, New York (2006).
29. Z. Yaqoob et al., "Methods and application areas of endoscopic optical coherence tomography," *J. Biomed. Opt.* **11**(6), 063001 (2006).
30. G. J. Tearney et al., "In vivo endoscopic optical biopsy with optical coherence tomography," *Science* **276**(5321), 2037–2039 (1997).
31. X. Li et al., "Imaging needle for optical coherence tomography," *Opt. Lett.* **25**(20), 1520–1522 (2000).
32. S. H. Yun et al., "Comprehensive volumetric optical microscopy in vivo," *Nat. Med.* **12**(12), 1429–1433 (2006).
33. H. L. Fu et al., "Flexible miniature compound lens design for high-resolution optical coherence tomography balloon imaging catheter," *J. Biomed. Opt.* **13**(6), 060502 (2008).
34. M. J. Gora et al., "Tethered capsule endomicroscopy enables less invasive imaging of gastrointestinal tract microstructure," *Nat. Med.* **19**(2), 238–240 (2013).
35. R. Kiesslich et al., "Technology insight: confocal laser endoscopy for in vivo diagnosis of colorectal cancer," *Nat. Clin. Pract. Oncol.* **4**(8), 480–490 (2007).
36. P. Kim et al., "In vivo wide-area cellular imaging by side-view endomicroscopy," *Nat. Methods* **7**(4), 303–305 (2010).

37. L. Qiu et al., "Multispectral scanning during endoscopy guides biopsy of dysplasia in Barrett's esophagus," *Nat. Med.* **16**(5), 603–606 (2010).
38. Laser Institute of America, *American National Standard for Safe Use of Lasers*, ANSI Z136.1-2007, American National Standards Institute, Inc., New York (2007).
39. L.-H. Wang, S. L. Jacques, and L.-Q. Zheng, "MCML-Monte Carlo modeling of photon transport in multi-layered tissues," *Comput. Methods Programs Biomed.* **47**(2), 131–146 (1995).
40. A. N. Bashkatov et al., "Optical properties of human skin, subcutaneous and mucous tissues in the wavelength range from 400 to 2000 nm," *J. Phys. D* **38**(15), 2543–2555 (2005).
41. J. M. Cannata et al., "Design of efficient, broadband single-element (20–80 MHz) ultrasonic transducers for medical imaging applications," *IEEE Trans. Ultrason. Ferroelectr. Freq. Control.* **50**(11), 1548–1557 (2003).
42. J. A. Jensen and N. B. Svendsen, "Calculation of pressure fields from arbitrarily shaped, apodized, and excited ultrasound transducers," *IEEE Trans. Ultrason. Ferroelectr. Freq. Control.* **39**(2), 262–267 (1992).
43. J. A. Jensen, "Field: a program for simulating ultrasound systems," *Med. Biol. Eng. Comput.* **34**, 351–353 (1996).
44. P. Lai, X. Xu, and L. V. Wang, "Dependence of optical scattering from Intralipid in gelatin-gel based tissue-mimicking phantoms on mixing temperature and time," *J. Biomed. Opt.* **19**(3), 035002 (2014).
45. P. Hajireza, W. Shi, and R. Zemp, "Label-free in vivo GRIN-lens optical resolution photoacoustic micro-endoscopy," *Laser Phys. Lett.* **10**(5), 055603 (2013).

Joon-Mo Yang received his PhD degree in physics from the Department of Physics and Astronomy, Seoul National University, Republic of Korea, in 2007. Currently, he is a research scientist in the Department of Biomedical Engineering at Washington University in St. Louis. His research develops novel imaging techniques based on optical and ultrasonic methods for their use in various biomedical applications.

Chiye Li received his BS degree in life sciences from the University of Science and Technology of China in Hefei, China, in 2007. Currently, he is a PhD student in biomedical engineering at Washington University in St. Louis. His research interests involve the application of photoacoustic imaging techniques in biological and medical studies.

Ruimin Chen received his BS degree in biomedical engineering from University of Electronics Science and Technology of China, Chengdu, China, in 2006, his MS degree in biomedical engineering from the University of Southern California (USC), Los Angeles, California, in 2008, and his PhD degree in biomedical engineering from USC in 2014, respectively. His research interests include high-frequency ultrasonic transducers and arrays, piezoelectric material characterization, and photoacoustic imaging.

Qifa Zhou received his PhD degree from Xi'an Jiaotong University, China, in 1993. Currently, he is a research professor at the NIH Resource Center for Medical Ultrasonic Transducer Technology and the Department of Biomedical Engineering at the University of Southern California. He is a fellow of SPIE, a senior member of the IEEE Ultrasonics, Ferroelectrics, and Frequency Control Society, and a fellow of the American Institute for Medical and Biological Engineering.

K. Kirk Shung received his PhD degree in electrical engineering from the University of Washington, Seattle, Washington, in 1975. He is a dean's professor in biomedical engineering at the Viterbi School of Engineering at the University of Southern California and has directed the NIH Resource Center for Medical Ultrasonic Transducer Technology since 1997. He is a life fellow of IEEE and a fellow of the Acoustical Society of America and American Institute of Ultrasound in Medicine.

Lihong V. Wang is the Beare Distinguished Professor at Washington University. His book entitled "Biomedical Optics" won the Goodman Award. He has published 395 journal articles with an h-index of 88 (>30,000 citations) and delivered 385 keynote/plenary/invited talks. His laboratory published the first functional photoacoustic CT and 3-D photoacoustic microscopy. He serves as the editor-in-chief of the *Journal of Biomedical Optics*. He was awarded OSA's C.E.K. Mees Medal, NIH Director's Pioneer Award, and IEEE's Biomedical Engineering Award.